

Qiangtang Plateau high pressure system and Indian summer monsoon co-regulated natural dust storm activity on the southern Tibetan Plateau during the Holocene



Canyi Zhang^a, Junhuai Yang^{a,*}, Fuyuan Gao^b, Haoyu Wang^a, Linkai Wang^a, Zhenqian Wang^c, Xin Liu^a, Wenxi Qu^a, Shuyuan Wang^d, Zixuan Chen^e, Youjun Wang^f, Fen Zhang^a, Dunsheng Xia^{a,1}

^a Key Laboratory of Western China's Environmental Systems (Ministry of Education), College of Earth and Environmental Sciences, Lanzhou University, Lanzhou 730000, China

^b School of Environment and Urban Construction, Lanzhou City University, Lanzhou 730070, China

^c Department of Physical Geography and Bolin Centre for Climate Research, Stockholm University, Stockholm 10691, Sweden

^d Key Laboratory of Ecological Safety and Sustainable Development in Arid Lands, Northwest Institute of Eco-Environment and Resources, Chinese Academy of Sciences, Lanzhou 730000, China

^e School of Geography and Tourism, Jiaying University, Meizhou 514015, China

^f College of Tourism and Environmental Resource, Zaozhuang University, Zaozhuang 277160, China

ARTICLE INFO

Editor: H Falcon-Lang

Keywords:

Holocene

Dust activity

Climate change

Aeolian deposits

Yarlung Zangbo River basin

ABSTRACT

The southern Tibetan Plateau (sTP) is an important source of global dust emissions and is also a region with a high concentration of human activities. Therefore, distinguishing climatic drivers of dust activity from anthropogenic influences is challenging. In this paper, we analyze a high-resolution aeolian sequence in the Yarlung Zangbo River basin on the sTP, which provides direct evidence of past dust accumulation. Quartz optically stimulated luminescence and radiocarbon dating indicate that this sequence accumulated during the early to middle Holocene, when human activity had a negligible influence on dust activity. We use grain size parameters including the sorting coefficient, residual grain size, grain size components determined by end-member modeling, and dust accumulation rate to reconstruct the history of natural dust storm activity. The results indicate a gradual decrease in dust storm activity from the early to middle Holocene. Combining modern meteorological data with climate simulations indicates that dust storm activity was co-regulated by the Qiangtang Plateau high (QPH) and the Indian summer monsoon (ISM). From the early to middle Holocene, with the gradual weakening of the QPH and ISM, both the near-surface wind intensity and the supply of dust materials decreased, which contributed to the decrease in dust storm activity. Overall, our findings provide new insights into the natural forcing mechanisms behind Holocene dust storm activity in this high-altitude region.

1. Introduction

The Tibetan Plateau (TP), known as Earth's "Third Pole" (Qiu, 2008), serves as both a major dust source and a key "transfer station", exerting profound influences on regional and global atmospheric processes (Liu et al., 2022b). Dust emissions from the TP significantly impact regional ecosystems, air quality, and socioeconomic activity (Xu et al., 2018; Wang et al., 2021b). Additionally, high-altitude dust transport alters global climate systems by altering the radiative forcing (Lambert et al.,

2013; Shaffer and Lambert, 2018; Kang et al., 2020), regulating biogeochemical cycles (Mahowald, 2011; Lambert et al., 2015; Zan et al., 2023), and influencing cloud microphysics (Chen et al., 2024). As a crucial component of the Asian water tower, the southern TP (sTP) sustains a large proportion of the human population of the plateau and also contains extensive aeolian deposits (Wang et al., 2024; Yang et al., 2025). Its dust emissions significantly influence the downwind terrestrial and marine environments in the Northern Hemisphere (Zan et al., 2023). Therefore, investigating the evolution and driving mechanisms of

* Corresponding author.

E-mail address: yangjh19@lzu.edu.cn (J. Yang).

¹ Deceased

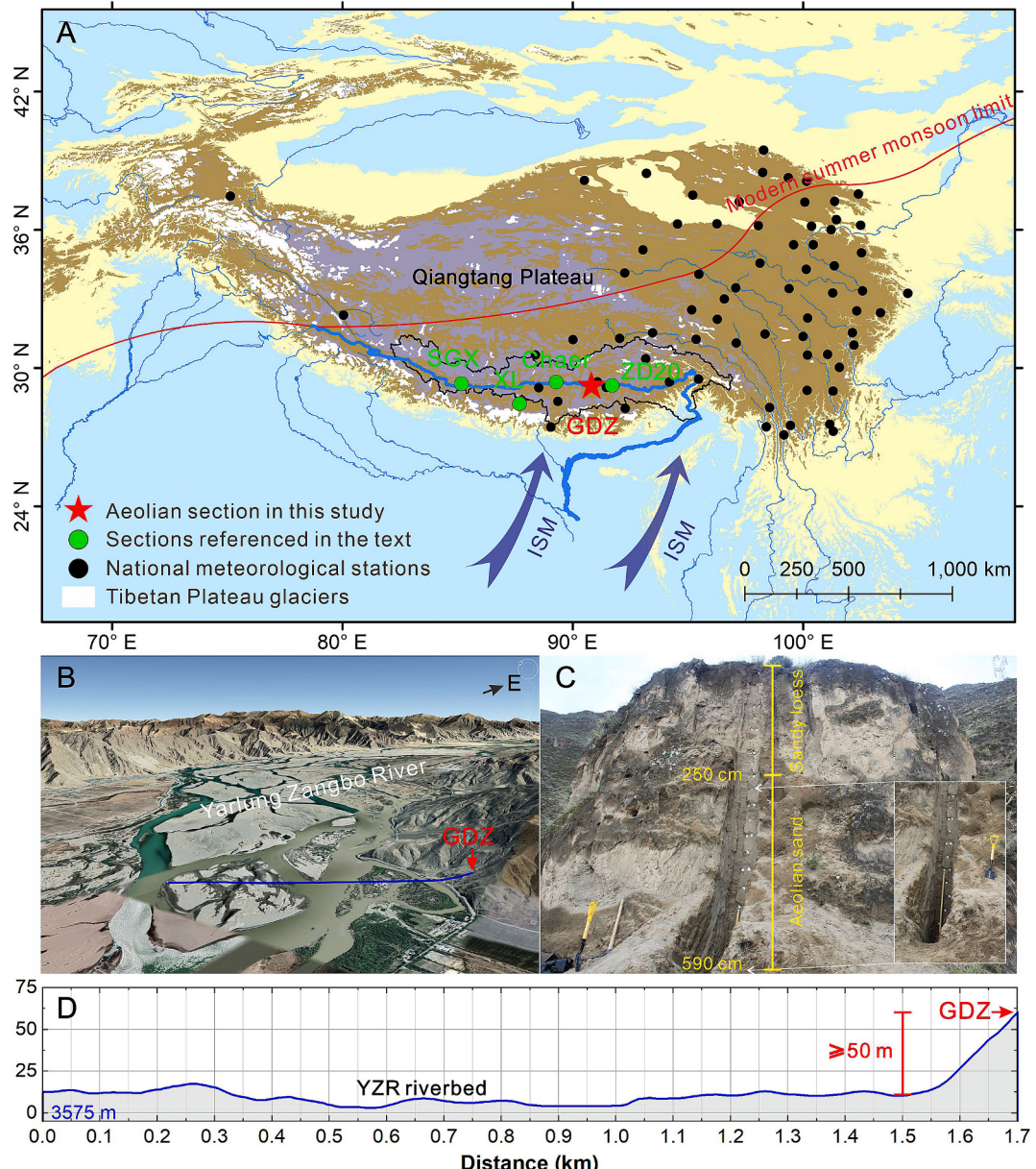


Fig. 1. (A) Locations of the studied and referenced aeolian sections, and 70 national meteorological stations. Detailed information about the sections is given in Table S1. Data of the modern summer monsoon limit are from Chen et al. (2019). (B) Satellite imagery and topographic features near the GDZ section. (C) Lithological characteristics of the GDZ section. (D) Topographic profile showing the elevation relationship between the section and the riverbed. The cross-section is shown in Fig. 1B.

dust activity in this region is essential for understanding the relationship between dust activity and the regional and global climate, as well as its current and future environmental status.

The evolution of Holocene dust activity on the sTP is debated, leading to inconsistencies in the interpretation of its driving mechanisms. For example: (1) A high-resolution lake sediment record from the sTP suggested a gradual increasing trend in dust activity throughout the Holocene, primarily controlled by the mid-latitude Westerlies (MLW) (Liu et al., 2024a); and (2) an integrated analysis of six Holocene aeolian records from the Yarlung Zangbo River (YZR) basin indicated a weakening trend in dust activity from the early to middle Holocene, followed by an increase in the late Holocene. Based on a modern process study it was suggested that regional temperature changes, modulated by cold-season insolation and ice volume, regulated the Holocene dust activity in this region via their influence on near-surface winds (Yang et al., 2024). The discrepancy between these two patterns may result from two

factors. Firstly, differences in sedimentary records and proxy interpretations could lead to differences in the patterns and mechanisms of reconstructed dust activity. Secondly, the potential influence of human activities on the sTP further complicates the dynamics of dust activity. Therefore, to accurately identify the natural drivers of dust activity, it is essential to focus on periods with minimal human influence and to use continuous sedimentary records with well-established proxies of dust activity. Previous studies suggest that human activities have significantly impacted the dust activity on the sTP mainly since the late Holocene (Cheng et al., 2023; Wang et al., 2024). Hence, dust activity during the early to middle Holocene was likely governed primarily by climatic factors. The YZR on the sTP contains abundant sand sources (Dong et al., 2017), favorable depositional conditions, and strong wind dynamics (Yang et al., 2020), resulting in the widespread distribution of well-preserved aeolian sand and loess deposits (Liu et al., 2024b). These deposits primarily accumulated during the Holocene and they provide

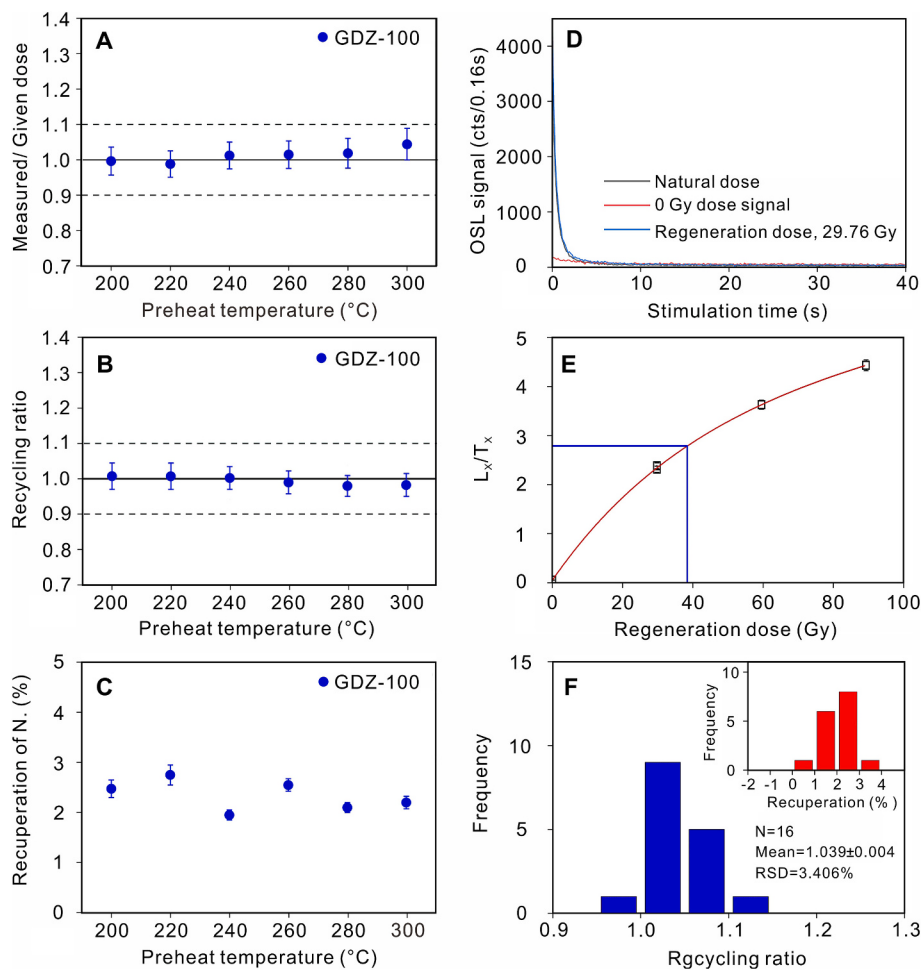


Fig. 2. (A–C) DRT results for representative sample GDZ-100. (D–E) Decay and growth curves of sample GDZ-100, respectively. (F) Recycling and recuperation data for all measured aliquots from the GDZ section.

direct evidence of TP dust activity in the past (Stauch, 2015; Ling et al., 2020; Yang et al., 2025).

In this study, we systematically analyzed a newly identified early to middle Holocene aeolian section in the YZR basin on the sTP. Additionally, we integrated data from four previously published aeolian sections in the same region to comprehensively investigate the regional characteristics of dust activity during the early to middle Holocene. We used grain size parameters including the sorting coefficient, residual grain size, grain size components determined by end-member modeling analysis (EMMA), and dust accumulation rate (DAR) to reconstruct the evolution of dust activity and to explore its potential driving mechanisms. Our findings increase our understanding of the natural variability of dust storm activity in this region, and they provide improved insights into dust transport processes and their responses to regional and global climate change.

2. Study area and aeolian sections

The YZR originates in the northern foothills of the Himalayas in the southwestern TP (Yao et al., 2010), and flows eastward across the southern plateau. The climate of this basin is primarily influenced by the interaction between the Indian summer monsoon (ISM) and the MLW (Gao et al., 2022a) (Fig. 1A). Both precipitation and temperature decrease from west to east across the basin (Ling et al., 2023; Yang et al., 2025). Additionally, both the mean annual wind speed and the frequency of sand-transporting winds decrease progressively downstream, displaying pronounced seasonal variations, with higher wind speeds

during winter and spring, which enhance the dust transport capacity (Yang et al., 2020). The YZR basin features heavily braided river channels, which significantly influence sedimentary processes. During the summer, intense precipitation leads to rising water levels, facilitating the transport of large volumes of fluvial sediments. In contrast, in winter, falling water levels expose the central bars and floodplains, which provide abundant material sources for aeolian deposits. Under the combined influences of the near-surface winds and fluvial processes, aeolian sediments are widely distributed across river terraces, slopes, hilltops, valley floors, and the windward slopes along both riverbanks (Dong et al., 2017; Yang et al., 2025).

The Gangduzhen (GDZ) section ($29^{\circ}16'09''$ N, $90^{\circ}49'00''$ E, 3641 m a.s.l.), with a total thickness of 590 cm, is located on the southern bank of the middle reaches of the YZR and is ~50 m above the riverbed (Fig. 1B, D). We collected bulk sediment samples at 2-cm intervals, resulting in a total of 295 samples (Fig. 1C). Additionally, seven samples were collected for optically stimulated luminescence (OSL) dating, and one paleosol sample was collected for accelerator mass spectrometry (AMS)¹⁴C dating. The lithology of the GDZ section, from top to bottom, is as follows: 0–30 cm, compact sandy loess with a loose texture, abundant plant roots, and mica; 30–50 cm, compact sandy loess with a small quantity of plant roots; 50–150 cm, compact sandy loess with abundant calcium nodules; 150–250 cm, compact sandy loess containing calcareous cement; 250–380 cm, aeolian sand with a high concentration of reflective minerals (possibly mica); 380–450 cm, relatively loose and coarse-grained aeolian sand; 450–590 cm, loosely deposited aeolian sand with a large quantity of gravel at the base.

Table 1

OSL results for seven samples from the GDZ section on the sTP.

Sample No.	Water content (%)	U (ppm)	Th (ppm)	Rb (ppm)	K (%)	Dose rate (Gy/ka)	OSL age (ka)
GDZ-25	20 ± 5	3.30	17.00	N/D	2.00	4.10 ± 0.10	4.60 ± 0.20*
GDZ-100	20 ± 5	1.98 ± 0.3	16.77 ± 0.9	106.59 ± 5	2.07 ± 0.04	4.15 ± 0.22	8.71 ± 0.48
GDZ-200	20 ± 5	1.73 ± 0.3	17.81 ± 0.9	116.89 ± 5	2.01 ± 0.04	4.09 ± 0.21	10.51 ± 0.58
GDZ-250	20 ± 5	3.00	16.30	N/D	1.90	3.90 ± 0.10	9.6 ± 0.50*
GDZ-350	20 ± 5	1.55 ± 0.3	18.16 ± 0.9	123.77 ± 5	2.22 ± 0.04	4.22 ± 0.22	10.94 ± 0.60
GDZ-450	20 ± 5	1.44 ± 0.3	12.83 ± 0.7	117.65 ± 5	2.3 ± 0.04	3.90 ± 0.20	11.52 ± 0.73
GDZ-550	25 ± 5	2.50	14.10	N/D	1.90	3.60 ± 0.10	11.80 ± 1.20*

Note: "N/D" indicates that no data are available. OSL results with * were dated at the Luminescence Research Laboratory of Linyi University, China; the rest were measured at the Luminescence Dating Laboratory of Shantou University, China.

Table 2AMS ^{14}C results for one sample from the GDZ section on the sTP.

Sample No.	Lithology	Material	^{14}C age (a BP)	Calendar age (cal a BP)	IRMS $\delta^{13}\text{C}$ (‰)
GDZ-10	Sandy loess	Bulk organic sediment	4180 ± 30	4691.5 ± 76.5 (71.9 %)	-20.0

For comparative analysis, we also selected four representative Holocene aeolian sequences on the sTP. Sequence selection adhered to four criteria: (1) the sequence covered the interval from 12.8 ka to 4.2 ka, consistent with the interval represented by our section; (2) the thickness of the sequence exceeded 180 cm, which ensured a relatively high sediment accumulation rate; (3) the chronology was well-constrained with at least three age control points per section; and (4) there were no significant erosional discontinuities.

3. Methods

3.1. OSL and AMS ^{14}C dating

OSL dating was conducted in the Luminescence Dating Laboratory of Shantou University and the Luminescence Research Laboratory of Linyi University, China. All samples were preprocessed under subdued red light, following the standard preparation procedures described by Aitken (1998). For measurements of the contents of uranium (U), thorium (Th), potassium (K), rubidium (Rb), and water, ~2–3 cm of sediment was carefully removed from both ends of each sample cylinder. The remaining sediment was wet-sieved to extract the 63–90 μm quartz fraction, which was then subjected to a series of chemical treatments: 10 % HCl to remove carbonates, 30 % H_2O_2 to remove organic matter, and 40 % HF for 60 min to remove feldspar contaminants and the alpha-irradiated outer layer. A final 10 % HCl treatment for 30 min was applied to dissolve any fluoride precipitates. The purified quartz grains were then mounted on 10-mm stainless steel discs using silicone oil for

purity assessment. Infrared stimulation (Duller, 2003) was employed to verify the quartz purity and additional etching was conducted if necessary. For samples that passed the purity test, the equivalent dose (D_e) was determined using the Single Aliquot Regenerative protocol (Murray and Wintle, 2000), combined with the Standard Growth Curve approach (Lai, 2006). All measurements were performed with a Risø TL/OSL-DA-20 reader equipped.

The concentrations of U, Th, and Rb were measured using inductively coupled plasma optical emission spectrometry, while K concentrations were determined using inductively coupled plasma mass spectrometry. These analyses were performed at the Xi'an Geological Survey Center, Shaanxi Province, China. The cosmic ray dose rate was calculated based on the sample burial depth, altitude, and geomagnetic latitude, following the method of Prescott and Hutton (1994). Accounting for variations in water content due to burial, sampling, and transport, an uncertainty of ±5 % was used as the water content, according to the previous study in this region (Yang et al., 2021).

AMS ^{14}C dating of bulk organic matter was performed by Beta Analytic (Florida, USA). The ages were calibrated using CALIB 8.1.0 with the INTCAL20 dataset (Reimer et al., 2020). This integrated approach combining AMS ^{14}C and OSL dating techniques enabled the establishment of a robust and well-constrained chronological framework for the GDZ section which was critical for interpreting the timing and dynamics of aeolian deposition during the Holocene.

3.2. Grain size, sorting coefficient, residual analysis, and EMMA

Grain size analysis is a fundamental tool for reconstructing the history of dust activity from aeolian sediments. Sample preparation for grain size analysis was as follows: removal of organic matter with 10 mL of 30 % H_2O_2 , and then of carbonates with 10 % HCl. After immersion in deionized water for 12 h, the supernatant was siphoned off and 10 mL of 0.05 mol/L $(\text{NaPO}_3)_6$ was added as a dispersant. The samples were further dispersed using an ultrasonic shaker. Grain size distributions were measured using a Malvern Mastersizer 2000 laser particle size analyzer (Malvern Panalytical Ltd., UK), following the procedures outlined by Lu and An (1998). All analyses were conducted at the Key Laboratory of Western China's Environmental Systems (Ministry of Education), Lanzhou University, China. The sorting coefficient was calculated from the grain size parameters, following Folk and Ward (1957).

The residual grain size was calculated following Kang et al. (2022a). Specifically, a time series of the coarse fraction content of each section was obtained by linear interpolation and then smoothed using a 50-year moving average. Subsequently, the residual grain size was obtained by subtracting the smoothed values from the interpolated data, expressed as:

$$RGS = C_i - C_s \quad (1)$$

where RGS represents the residual grain size, C_i is the interpolated coarse fraction content, and C_s is the smoothed value calculated as:

$$C_s = \frac{1}{w} \sum_{j=t-\frac{w}{2}}^{t+\frac{w}{2}} C_i(j) \quad (2)$$

where w is the time window (adjustable according to the study's needs), t is the specific time point at which residual grain size is calculated, and j is the index of each time point within the window (summation variable).

EMMA is a quantitative approach used to decompose grain size distributions into distinct components, which can provide critical insights into sediment transport mechanisms, depositional environments, and transport distances (Weltje, 1997). In this study, EMMA was applied to the early to middle Holocene aeolian sequence to characterize changes in dust activity. The end-member components and their relative contributions in each sample were determined using AnalySize (Paterson and Heslop, 2015). In the EMMA process, the grain size

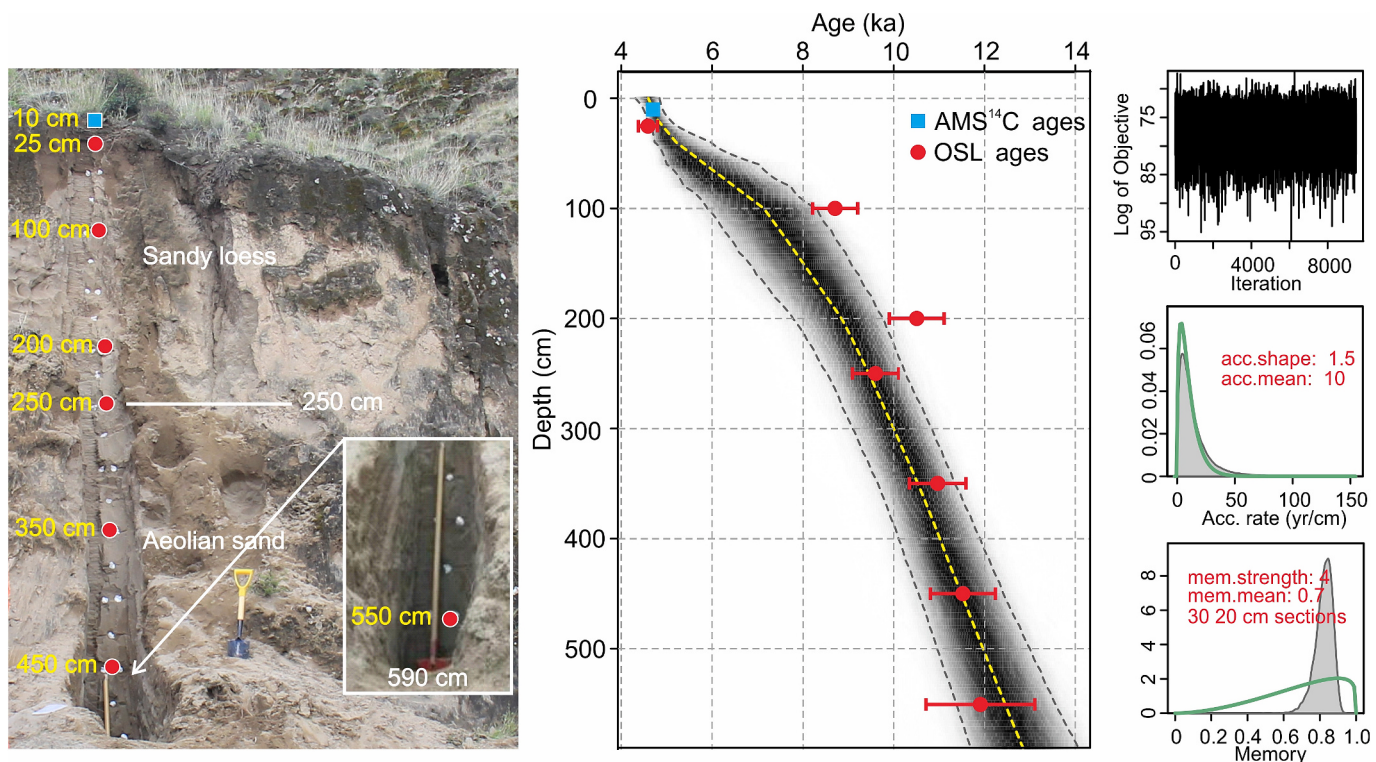
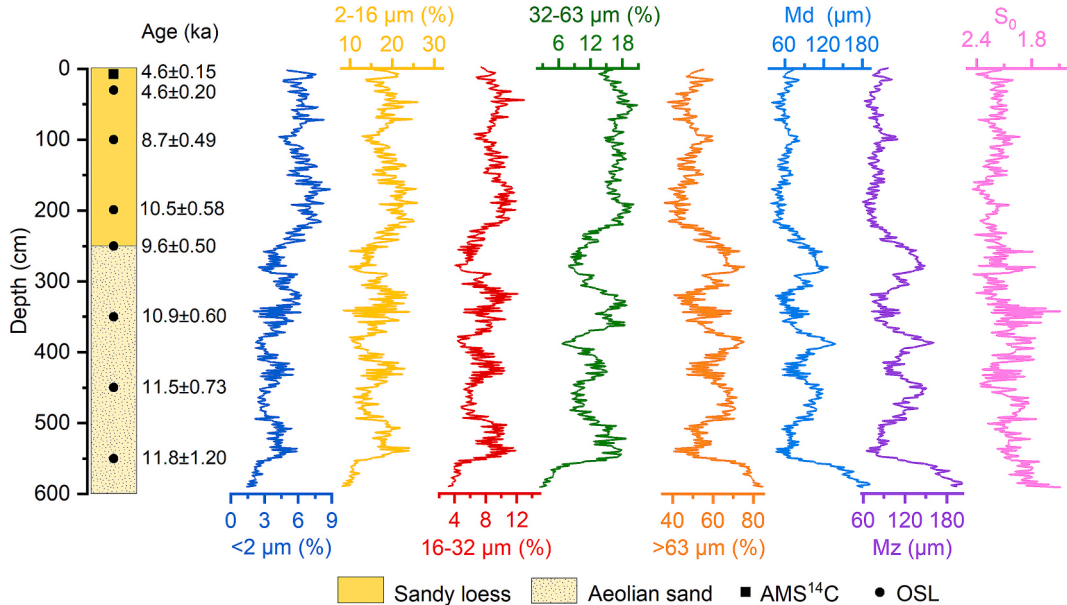


Fig. 3. Lithology and Bayesian age-depth model for the GDZ section.



distributions of the sediment samples were fitted using the Gen. Weibull function. The number of end-members (EMs) was initially set to between 1 and 10. To determine the optimal number of EMs, we evaluated the results based on linear correlation coefficients (R^2), angular deviation (θ), and the degree of correlation among the end-members. A higher R^2 (typically > 0.9) and a lower θ ($< 5^\circ$) indicate a better model fit (Paterson and Heslop, 2015).

3.3. Dust accumulation rate

Based on the chronologies obtained for each section, a Bayesian age-depth model was constructed using the Bacon 2.2 program in R (Blaauw and Christen, 2011), providing a depth-series resolution of 1 cm. The DAR at a resolution of 0.05 kyr for each section was estimated by computing the first derivative of the age-depth sequence. On this basis, the records of coarse fraction content, mean grain size (Mz), and DAR of each section were standardized using Z-scores (Zhao et al., 2022) to eliminate differences in scale among the variables. The weighted

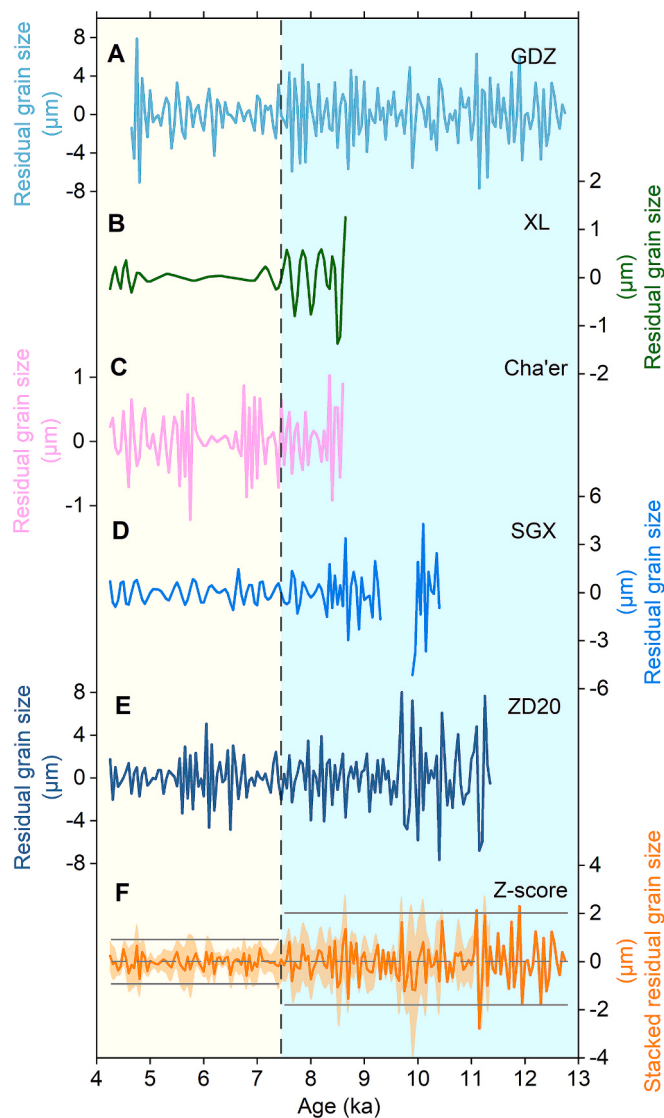


Fig. 5. (A–F) Residual grain size (interpolated minus smoothed) records from five sections. The stacked result is shown in Fig. 5F. The light-yellow and light-blue intervals represent warm and cold intervals, respectively.

average of these standardized sequences was then calculated. Z-scores are calculated as:

$$Z = (X - X_{\text{mean}})/X_{\text{SD}} \quad (3)$$

where Z represents the standardized interpolated data at 0.05 kyr intervals, X_{mean} is the mean of the grain size/DAR, and X_{SD} is the standard deviation of the grain size/DAR. We calculated the mean of the combined standardized grain size/DAR series from all sections to generate stacked mean grain size/DAR records for the sTP. Calculating the standard deviation of these standardized sequences provided a corresponding error estimate.

3.4. Meteorological data analysis and Trace-21 ka climate simulation

We selected 70 meteorological stations with a uniform spatial distribution and low missing data rates across the TP. These data are from the climate database provided by the China National Meteorological Information Center (CMIC, <http://data.cma.cn/en>). The dataset comprises daily mean wind speed and temperature records spanning the interval from 1973 to 2013. Daily mean wind speed was computed as the average of observations recorded at 02:00, 08:00, 14:00, and 20:00

Beijing Standard Time. To eliminate the influence of non-climatic factors, such as station relocations and anemometer aging, the Climatol package provided by Guijarro (2018) (<http://www.climatol.eu/>; last accessed on June 1, 2025) was employed for data quality control, homogenization, and replacement of missing data. This method was successfully applied in previous studies (Zhang et al., 2024a). Based on the preprocessed data from 70 meteorological stations across the TP, we used the Pearson correlation coefficient to evaluate the relationship between temperature and wind speed variability. In addition, kriging interpolation was applied to reveal the spatial distribution of wind speeds under different cold-season temperature conditions.

Additionally, we utilized the Trace-21 ka climate model to simulate the near-surface wind speed and mean temperature during the cold season (December to April of the following year) (Yang et al., 2024) on the sTP from the early to middle Holocene. This advanced atmosphere-ocean coupled model simulates climate evolution over the past 21,000 years by integrating a comprehensive set of external forcings, including solar radiation, greenhouse gas concentrations, continental ice volume, and meltwater fluxes (Liu et al., 2009).

4. Results

4.1. Chronology

The preheat plateau test and dose recovery test (DRT) were conducted on representative sample GDZ-100. The DRT results (Fig. 2A–C) show that the measured-to-given dose ratios remained stable within the preheat temperature range of 220–260 °C. The recycling ratio fell between 0.90 and 1.10, while the recuperation was <5 %. The OSL signal rapidly declined to background levels within 2 s of stimulation, indicating the dominance of the fast component (Fig. 2D). The growth curve figure demonstrates a continuous signal increase up to a dose of 90 Gy (Fig. 2E). The recycling ratios of all quartz aliquots are concentrated between 0.9 and 1.2, with an average of 1.039 ± 0.0004 and relative standard deviation (RSD) of 3.406 %. Additionally, more than 95 % of the quartz aliquots had recuperation values <5 % (Fig. 2F).

The quartz OSL dating and AMS ^{14}C dating results for the GDZ section are presented in Tables 1–2. The OSL ages generally increase with depth, ranging from 4.6 ± 0.2 ka at 20 cm to 11.8 ± 1.2 ka at 550 cm. Bayesian age-depth models provide more precise and reasonable estimates for sediment chronologies (Blaauw et al., 2018). We established a chronological framework for the GDZ section using Bacon age-depth modeling (Blaauw and Christen, 2011), incorporating seven OSL ages and one AMS ^{14}C age (Fig. 3). Linear extrapolation was applied to determine ages for the depth intervals of 0–10 cm and 550–590 cm. The results indicated that the basal age of the section is ~12.8 ka, with accumulation continuing into the middle Holocene (Fig. 3).

4.2. Grain size results

Depth series of the grain size parameters and sorting coefficient of the GDZ section are shown in Fig. 4. The variations in Mz and median grain size (Md) closely follow the changes in the $>63 \mu\text{m}$ fraction content, indicating that the grain size fluctuations within this section are primarily controlled by variations in the coarse particle content. The relatively high values of Mz (59.48–202.64 μm , average 101.46 μm) and Md (38.15–191.90 μm , average 80.44 μm) indicate that the sediments are generally coarse. This coarse grain size distribution may reflect the influence of high-energy aeolian processes, potentially associated with dust storm activity. The trend of the $>63 \mu\text{m}$ fraction also corresponds well with that of the sorting coefficient, further supporting the inference that the coarse fraction is a dependable proxy for near-surface wind strength and, by extension, the intensity of dust activity. The sorting coefficient ranges between 1.49 and 2.44, with an average of 2.11, indicating very poor sorting (Blott and Pye, 2001). Such poor sorting implies short transport distances and suggests that the sediments were

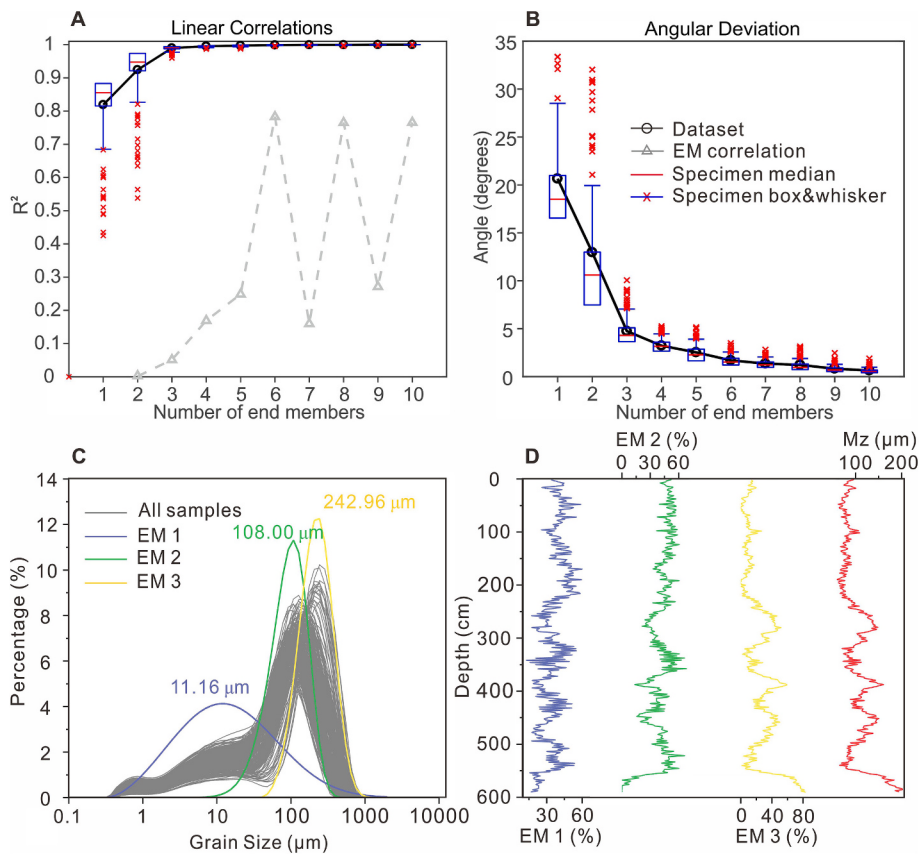


Fig. 6. (A–B) Linear correlations (R^2) and angular deviations (θ) for each EM, (C) grain size frequency distribution curves of all EMs. (D) Depth series of the three EMs and Mz for the GDZ section.

likely sourced from nearby rivers.

The residual grain size records and their stacked record indicate that all five sections had higher residual values during the early Holocene when the climate was colder (higher ice volume and lower winter temperature), and lower values during the middle Holocene when the climate was warmer (lower ice volume and higher winter temperature) (Fig. 5). Notably, there was a significant change in the amplitude of the residual grain size at ~ 7.5 ka (Fig. 5F), when the ice volume reached its lowest and the winter temperature increased significantly.

The EMMA results show that with the selection of three EMs, R^2 reached 0.99 (Fig. 6A), θ was 4.7 (Fig. 6B), and the correlation among the EMs was low ($R^2 = 0.051$), meeting the aforementioned optimization criteria. Therefore, EMMA yielded the optimum fitting results with a three EM model. The modal grain sizes of the three primary EMs were: EM1 (11.16 μm), EM2 (108.00 μm), and EM3 (242.96 μm) (Fig. 6C), and their variations are shown in Fig. 6D.

The integrated DAR records from representative Holocene aeolian sedimentary sequences show that, despite variations among the individual sections, the temporal trends are consistent (Fig. 7). During the early Holocene, DAR remained relatively high but with a gradual decreasing trend. In the middle Holocene, the DAR stabilized at lower levels, with subsequent section-specific increases of varying magnitude.

5. Discussion

5.1. Environmental implications of proxies and the history of dust storm activity

Grain size can be influenced by factors including sediment provenance, source-to-sink distance, and post-depositional processes including weathering and pedogenesis. However, geochemical analyses

have shown that aeolian sediments in the YZR basin are derived predominantly from local sources including nearby dunes, fluvial deposits, alluvial fans, and lithic materials (Ling et al., 2021; Ling et al., 2022). Additionally, the coarse fraction of the sediments is minimally affected by post-depositional weathering and pedogenesis (Yang et al., 2021; Yang et al., 2023). Therefore, when the effects of these factors are minimized, the grain size may provide a robust proxy for assessing changes in the intensity of dust activity in this region. The grain size distributions of the GDZ section indicate domination by variations in coarse particles (Fig. 4). Previous studies have demonstrated that the $>63 \mu\text{m}$ fraction and the Mz are effective proxies for near-surface wind intensity and they have been successfully applied in the Chinese Loess Plateau, the eastern region of the Central Asian Arid Zone, and on the sTP (Lu and An, 1998; Gao et al., 2021; Yang et al., 2024). Furthermore, Pan et al. (2014) reported that $>250 \mu\text{m}$ particles can serve as an indicator of coarse grains that are sensitive to strong dust activity in the XL section. Therefore, the coarse fraction reliably indicates variations in dust activity (Yang et al., 2024). The residual grain size is calculated by removing the long-term trend from the coarse fraction record, thereby isolating short-term, high-frequency fluctuations (Kang et al., 2022a). Therefore, the residual grain size reflects high-frequency amplitude variations in dust activity. Previous studies of dust dynamics have shown that $>63 \mu\text{m}$ particles are generally transported via saltation and short-distance suspension (Zhao et al., 2016). The GDZ section is located ~ 50 m from the riverbed (Fig. 1D), and thus we infer that the site may have accumulated dust materials mobilized from the river valley during dust storm events. These particles were likely transported over a certain distance and eventually deposited after obstruction by local topographic features such as the surrounding mountain slopes.

The sorting coefficient describes the width of the grain size distribution and is an indicator of aeolian transport dynamics. Poor sorting in

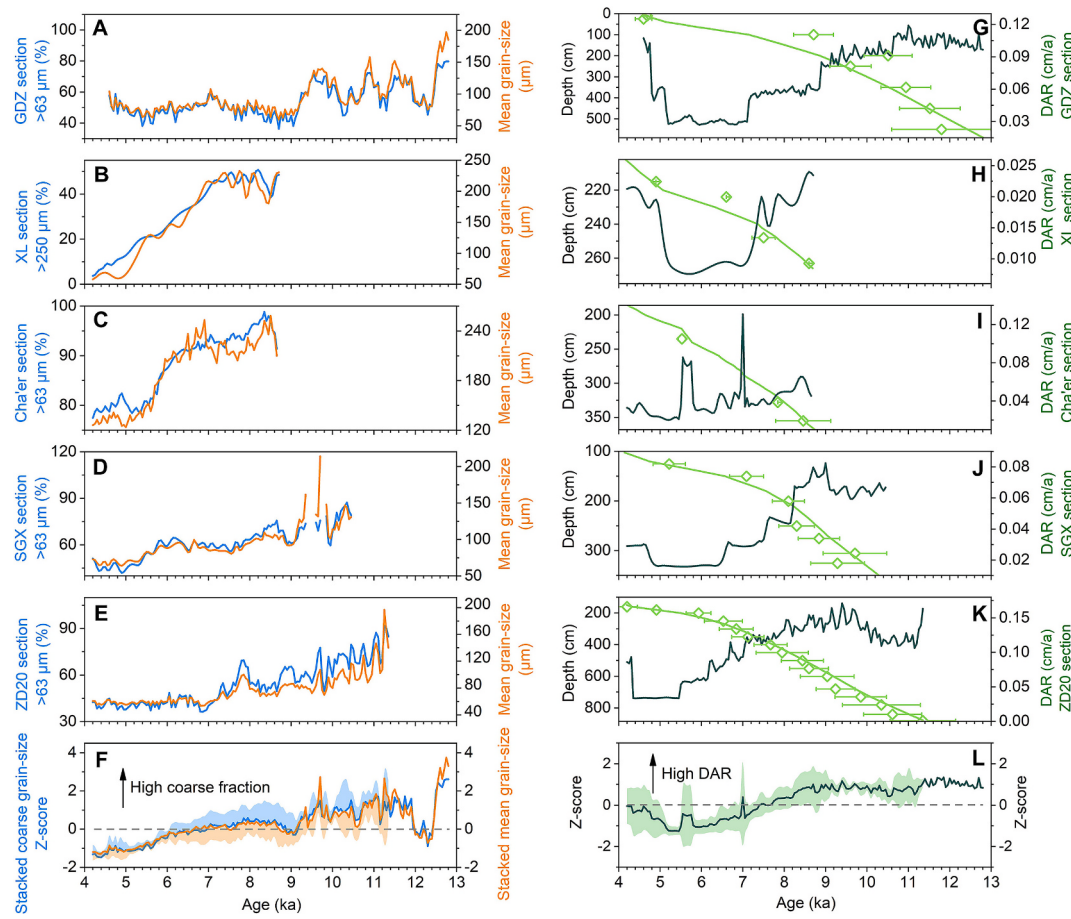


Fig. 7. (A–F) Time series of coarse grain size (blue line) and Mz (orange line) from five sections on the sTP. (G–L) Age-control points (light green lines) and DAR records (dark green line) for the five sections. The stacked results for the five aeolian records are shown in Figs. 7F and 7L.

suspended sediments mainly results from mineral density contrasts, whereas strong near-surface winds can transport both coarse and fine particles, thereby improving sorting and lowering the coefficient (Cheng et al., 2020). In the GDZ section, sorting remains very poor, but its temporal changes align with variations in Mz and the coarse fraction (Fig. 4), suggesting wind strength as the primary control. Thus, relative changes in the sorting coefficient provide a dependable proxy for dust activity intensity in this region. Unlike other indicators such as the Mz, the sorting coefficient is largely unaffected by variations in dust source location or vegetation cover. Therefore, it is a more sensitive proxy for detecting changes in near-surface wind strength and dust activity, particularly during periods with weaker winds (Cheng et al., 2022; Cheng et al., 2025).

EMMA is a useful tool in grain size analysis and the reconstruction of aeolian processes and can effectively distinguish components with different origins, transport mechanisms, and transport distance (Song et al., 2024). In the GDZ section, the variation of the EM 1 component (modal grain size of 11.16 µm) is similar to that of the 1.c.2 component type (2–10 µm) proposed by Vandenberghe (2013), which reflects the influence of the mid-latitude Westerlies. However, in the GDZ section the variation of the EM 1 component differs from that of the 1.c.2 component, which may result from the combined influences of fine particle transport by the mid-latitude Westerlies and local suspended dust produced during weathering and pedogenesis (Song et al., 2024).

In summary, we conclude that the EM 1 component of the GDZ profile is mainly transported by the WLM and can be regarded as a continuous background dust supply during non-dust storm processes (Vandenberghe, 2013). This inference is supported by the EMs of other loess sections, which have similar modal grain sizes ranging from ~10 to

~13 µm (Jia et al., 2018; Wang et al., 2019; Duan et al., 2020). Additionally, pedogenesis may also contribute to EM 1 (Gao et al., 2022b). However, a previous study of other sections within the YZR basin found that pedogenic processes in this region are relatively weak (Yang et al., 2023). Therefore, aeolian activity likely played the dominant role in sediment accumulation at the GDZ section. Components EM 2 (modal grain size of 108.00 µm) and EM 3 (modal grain size of 242.96 µm) in the GDZ section have a pronounced inverse relationship, which may reflect different aspects of the same dynamic process. Atmospheric dynamics research and empirical observations indicate that coarse particles with diameters of 100–500 µm are primarily lifted by wind and are typically transported via near-surface saltation (Pye, 2015). Under extreme dust storm conditions, coarse particles can even be transported for hundreds of kilometers (Tsoar and Pye, 1987). The sediments in the study area primarily originate from sandy materials previously accumulated in nearby river terraces and exposed river islands, with transport distances typically ranging from several hundred meters to a few kilometers. Therefore, components EM 2 and EM 3 may collectively indicate the history of strong near-surface winds and dust storm evolution on the sTP. The variation of EM 3 in the GDZ section closely follows that of Mz and the >63 µm fraction, with strong correlations observed among these proxies (Figs. 6D and S1), indicating that the GDZ sediments were predominantly transported by strong near-surface winds and episodic dust storm activity.

Previous studies have shown that the DAR is a sensitive climatic indicator, with dust deposition increasing during cold and arid periods and decreasing significantly during warm and humid periods (Guo et al., 2001). However, a comparison of the DAR records of different sections with their corresponding Mz and coarse fraction contents reveals that

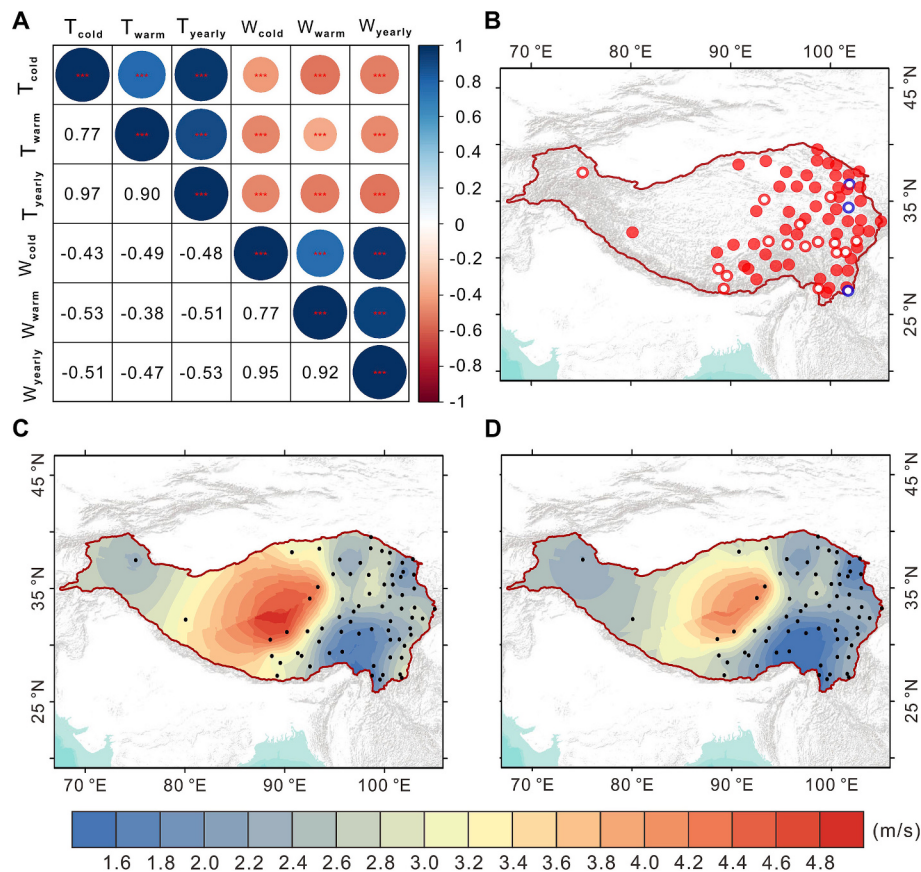


Fig. 8. (A) Correlation between temperature and wind speed on seasonal and annual scales. Blue/red indicates positive/negative correlation. *** denotes statistical significance ($p < 0.001$). $T_{\text{cold}}/W_{\text{cold}}$, $T_{\text{warm}}/W_{\text{warm}}$, and $T_{\text{yearly}}/W_{\text{yearly}}$ represent the temperature/wind speed in the cold season, warm season, and the whole year. (B) Correlation between near-surface wind speed and average temperature over the TP. Blue/red indicates positive/negative correlation, solid dots represent the significance level ($p < 0.05$), and open circles indicate no significance. (C) Near-surface wind speed during the five years with the lowest cold-season temperatures (1975, 1977, 1982, 1985, 1994). (D) Near-surface wind speed during the five years with the highest cold-season temperatures (1998, 2004, 2005, 2008, 2009). (For interpretation of the references to colour in this figure legend, the reader is referred to the web version of this article.)

the temporal trends of DAR do not entirely align with those of the grain size parameters (Fig. 7). This suggests that while the DAR is influenced by aridity and wind strength, it is also modulated by multiple environmental factors, including vegetation cover and source area characteristics (Kang et al., 2022b). Under similar wind conditions, vegetation cover plays a crucial role in controlling wind erosion and DAR variations. A reduced vegetation cover increases the extent of exposed surface areas, making surface sediments more susceptible to wind erosion which increases the DAR. Additionally, recent studies highlight that DAR variations are not controlled solely by climatic factors, as hydrological processes also play a critical role in dust transport and deposition. While climatic warming may reduce wind erosion, it can simultaneously enhance water erosion, increasing the sediment transport capacity of river and making the dust supply dependent not only on wind transport but also on hydrodynamic processes (Peng et al., 2022). Therefore, changes in DAR are driven by the combined effects of wind strength, aridity, vegetation cover, and hydrological processes. Integrating DAR with grain size indicators contributes to an improved understanding of the evolution of dust activity in the study area.

Although the detailed variations among the $>63 \mu\text{m}$ fraction, sorting coefficient, residual grain size, EM 3, and DAR differ slightly, their overall trends are consistent, indicating that these proxies reliably reflect changes in dust activity intensity. Based on their combined analysis, we reconstructed the evolution of dust storm activity on the sTP from the early to middle Holocene. During the early Holocene, the coarse fraction content, sorting coefficient, and residual grain size remained high, with elevated EM3 and DAR values (Figs. 4–7),

indicating strong dust storm activity. Dust storm activity decreased markedly in the middle Holocene, evidenced by reductions in the coarse fraction content, sorting coefficient, and residual grain size amplitude, as well as by decreases in EM3 and DAR (Figs. 4–7). Overall, Holocene dust storm activity intensified in the early Holocene and weakened in the middle Holocene.

5.2. Primary controls on dust activity

A recent study demonstrated the primary control of temperature on dust activity on the TP (Long et al., 2025). To better understand how temperature influences aeolian processes, we examined the modern relationship between mean near-surface wind speed and temperature across the plateau. This analysis offers new insights into the key climatic factors that governed dust activity during the early to middle Holocene.

Analysis of modern meteorological data reveals a significant negative correlation between mean wind speed and temperature across 70 meteorological stations on the TP (Fig. 8B). Among them, 67 stations show a negative correlation, while only 3 show a positive correlation. Most of these correlations are statistically significant ($p < 0.05$). Notably, nearly all the stations on the sTP display a significant negative correlation. Further insights are provided by correlation heatmaps of the temperature and wind speed during the cold season, the warm season (June–August) (Yang et al., 2024), and on an annual timescale. These results resulted in a correlation coefficient of -0.43 between cold-season temperature and wind speed, -0.51 between cold-season temperature and annual wind speed, and -0.47 between warm-season wind speed

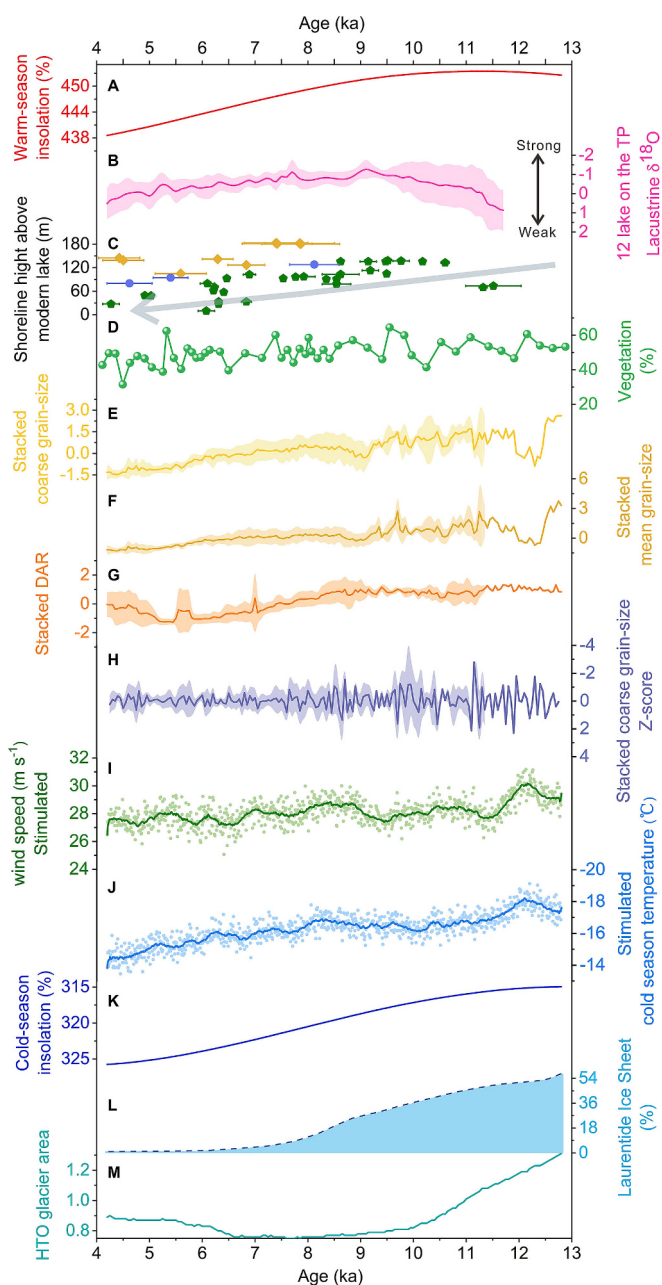


Fig. 9. Drivers of dust storm activity from the early to middle Holocene on the sTP. (A) Warm-season insolation at 30°N. (B) Composite $\delta^{18}\text{O}$ record derived from sedimentary records from 12 lakes on the sTP (Wu et al., 2022). (C) Lake-level reconstructions from Lake Ngangla Ring Tso (green pentagons) (Hudson et al., 2015), Lake Tangra Yumco (yellow rhomboids) (Rades et al., 2013; Rades et al., 2015), and Lake Zhari Namco (blue circles) (Chen et al., 2013). (D) Temporal variations in vegetation cover (Liu, 2023). (E–H) Stacked records of coarse fraction size, Mz, DAR, and residual grain size on the sTP (this study). (I–J) Simulated cold season near-surface wind speed and temperature using the TraCE-21 ka simulation (this study). (K) Cold-season insolation at 30°N. (L) Area of the Laurentide ice sheet (Dyke, 2004). (M) Ratio of past to present glacier area in the Himalayan-Tibetan Orogen (HTO) region (Yan et al., 2020). (For interpretation of the references to colour in this figure legend, the reader is referred to the web version of this article.)

and annual wind speed (Fig. 8A). This suggests that decreasing cold-season temperature is the dominant control on wind speed. Overall, a strong negative correlation exists between cold-season temperature and near-surface wind speed on the sTP, with the cold-season temperature being the dominant control of wind intensity. Given that near-surface

wind is the primary driver of dust activity, its variability directly influences dust transport. Therefore, changes in cold-season temperature indirectly regulate dust activity by modulating the wind speed.

The spatial distribution of mean wind speed across the TP (Fig. 8C, D) shows that the highest wind speeds occur near the Qiangtang Plateau, which gradually decrease towards the plateau's periphery, resulting in a steep wind speed gradient. This pattern is particularly pronounced during years with the lowest cold-season temperatures (Fig. 8C). The spatial distribution of dust activity intensity aligns with that of wind speed. Modern meteorological data and climate model simulations confirm that the Qiangtang Plateau experiences the most intense dust activity on the TP (Zhang et al., 2024b). Atmospheric dynamics and satellite observations corroborate these findings, identifying the Qiangtang Plateau as the primary dust emission region, with a major dust transport pathway extending eastward along the YZR basin on the sTP (Fang et al., 2004). The Qiangtang Plateau's elevated and relatively flat terrain facilitates the retention of cold air and the maintenance of a high-pressure system (Dong et al., 2010). In contrast, the narrower valley topography on the sTP may channel wind fields eastward or southward, regulating the dust transport. Based on these findings, we hypothesize that a relatively high-pressure system may develop near the Qiangtang Plateau due to a combination of topographic influences and thermal contrasts with the surrounding atmosphere. We term this system the Qiangtang Plateau high (QPH). During the cold season, the QPH significantly enhances near-surface wind speeds, influencing the transport and deposition of windblown sediments. Previous studies support the existence of the QPH. For instance, radiocarbon dating of dunes in the Puruogangri region indicated formation ages of 12.7–9.2 ka, which may have been linked to winter anticyclonic activity over the Qiangtang Plateau (Li et al., 2006).

Warm-season dust activity on the sTP is primarily regulated by the ISM. Sediments in the YZR basin are of local origin and are influenced by both aeolian and fluvial processes (Yang et al., 2025). Moisture influx during periods of strengthened ISM brings abundant precipitation to the sTP, leading to a rise in river levels and intensified fluvial erosion (Liu et al., 2022a). Concurrently, fluvial processes transport sediments from the upper to the middle and lower reaches, where they are subsequently deposited. In contrast, during the dry season, river levels fall, exposing fluvial sediments, thereby providing a sufficient sediment supply for dust activity.

Based on the foregoing analysis, the QPH primarily regulates the near-surface wind strength, providing the dynamic conditions necessary for dust mobilization, while the ISM controls sediment availability via its influence on precipitation and the vegetation cover. Together, these two systems modulate dust activity over the sTP.

5.3. Driving mechanisms of dust storm activity in the early to middle Holocene

Results from modern dust activity indicate that wind dynamics and precipitation jointly regulate sediment supply and transport on the sTP. To further elucidate the evolution and potential driving mechanisms of dust activity on the sTP during the early to middle Holocene, we integrated TraCE-21 ka simulations with regional dust records and key global paleoclimate records. Based on this comparative analysis we propose the primary driving mechanisms responsible for dust activity during the early and middle Holocene in this region.

During the warm season of the early Holocene, increased solar insolation at 30°N strengthened the ISM (Fig. 9A, B), causing the transport of substantial amounts of moisture into the sTP and abundant precipitation (Chen et al., 2020). This enhanced rainfall led to a significant rise in river levels (Fig. 9C), increased runoff, and intensified fluvial erosion, facilitating the transport of upstream sediments to the middle and lower reaches, where they accumulated in low-lying areas, forming extensive alluvial deposits (Chen et al., 2020; Yang et al., 2025). During this period, the high water level in the YZR basin left few or no

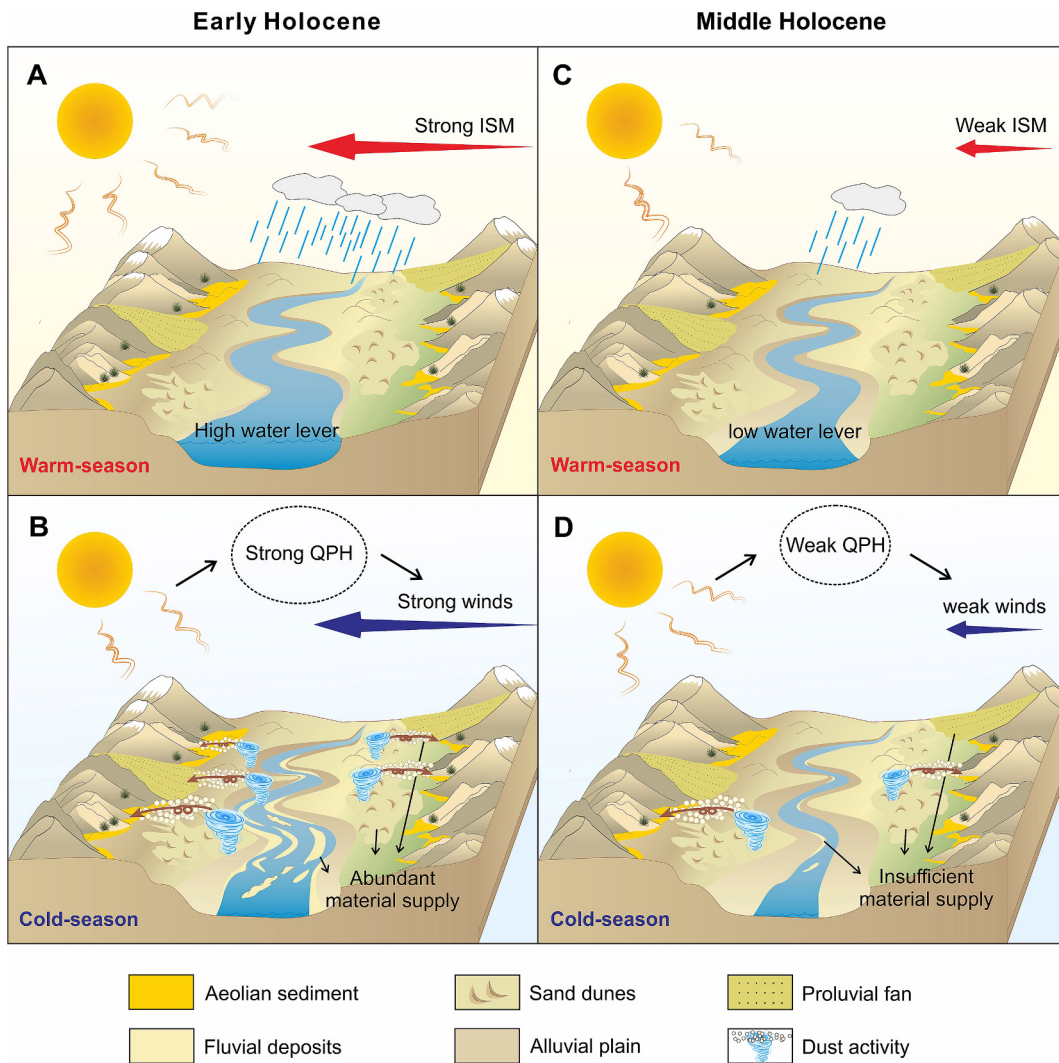


Fig. 10. Model of the evolution and driving mechanism of dust storm activity during the early to middle Holocene on the sTP. ISM: Indian summer monsoon; QPH: Qiangtang Plateau high.

channel bars or point bars exposed, whereas the subsequent fall in water levels during the cold season exposed these deposits (Wang et al., 2021a). Therefore, the substantial sediment accumulation during the warm season provided an ample sediment supply for cold-season dust transport, establishing the material basis for dust deposition. Additionally, increased precipitation promoted vegetation expansion (Fig. 9D), which may have actively contributed to dust deposition by trapping suspended airborne particles (Sun et al., 2007). Conversely, during the cold season of the early Holocene, insolation at 30°N was lower (Fig. 9K), and temperatures were also reduced (Fig. 9J). Extensive glaciation enhances the surface albedo, thereby reducing atmospheric temperatures above the ice surface and contributing to the formation of a pronounced glacial anticyclone (Cheng et al., 2025) (Fig. 9L, M). These factors together sustained a strong QPH and further intensified near-surface wind speeds (Fig. 9I). Previous studies have shown that near-surface wind is an important external forcing factor for dust activity (Yang et al., 2020); therefore, increased wind speed facilitated the remobilization of sediments. The coarse grain size, Mz, and DAR (Fig. 9E–G) exhibit antiphase variations with cold-season temperature (Fig. 9J), further indicating stronger dust storm activity under colder conditions. During the cold season, the amplitude of the residual grain size was also higher (Fig. 9H), consistent with the findings of Kang et al. (2022a). Overall, in the early Holocene (Fig. 10A, B), the ISM and QPH co-regulated dust storm activity on the sTP. A strong ISM during the

warm season provided sufficient sediment input via hydrodynamic processes, while during the cold season, the QPH enhanced near-surface wind speeds and thereby exerted a dynamic control on dust storm activity.

During the warm season in the middle Holocene, solar insolation at 30°N decreased substantially (Fig. 9A), which weakened the ISM (Fig. 9B) and reduced the moisture transport into the sTP. Consequently, the regional precipitation decreased, leading to a fall in river levels (Fig. 9C) and decreased fluvial erosion. Consequently, the transport of upstream sediments diminished, causing a substantial decrease in alluvial deposition which directly reduced the warm-season sediment supply. Additionally, the reduced precipitation also decreased the vegetation cover (Fig. 9D). Together, these changes greatly constrained the amount of sediment available for wind transport in the subsequent cold season, thereby suppressing dust storm activity. During the cold season of the middle Holocene, as solar insolation at 30°N increased (Fig. 9K), cold-season temperatures gradually rose (Fig. 9J). The Northern Hemisphere continental ice sheets retreated, and the glaciers on the sTP melted (Fig. 9L, M). These changes led to a gradual weakening of the QPH, resulting in reduced near-surface wind speeds (Fig. 9I). The declining wind strength reduced the capacity for surface sediment transport and further suppressed the dust storm activity. Furthermore, with the decreased warm-season sediment input, the reduced wind strength in the cold season was insufficient to mobilize

significant amounts of dust, resulting in a marked decrease in dust transport. Overall, compared to the early Holocene, both hydrodynamic and wind-driven processes weakened substantially in the middle Holocene (Fig. 10C, D), leading to a decline in dust storm activity. This is reflected in the reductions in grain size, DAR, and their amplitude of fluctuations in the studied sections at this time (Fig. 9 E–H).

In summary, dust storm activity on the sTP during the early to middle Holocene was jointly driven by warm-season sediment supply and cold-season wind dynamics, with dust storm intensity varying markedly under different climatic backgrounds. While our analysis of modern wind dynamics primarily considers temperature, it does not fully account for potential synergistic effects of other climatic and ecological variables. Future studies should incorporate multiple environmental drivers to better elucidate the mechanisms regulating dust storm activity across the TP and assess the broader applicability of this framework at regional to continental scales.

6. Conclusions

We analyzed the coarse fraction content, sorting coefficient, residual grain size, EMMA, and DAR records from five early to middle Holocene aeolian sections on the sTP. The results indicate that dust storm activity gradually weakened from the early to middle Holocene. By integrating modern meteorological data, TraCE-21 ka simulations, and global paleoclimate data, we found that this trend was primarily controlled by variations in temperature and precipitation. Increasing cold-season insolation and decreasing ice volume led to gradual warming, with temperature changes modulating the intensity of the QPH, thereby affecting near-surface wind strength and dust storm activity. During the warm season, the ISM primarily influenced sediment availability via its control on precipitation and vegetation cover. Collectively, these findings demonstrate that the QPH and ISM co-regulated natural dust storm activity on the sTP during the Holocene, with the QPH driving wind dynamics in the cold-season and the ISM controlling sediment supply in the warm season.

CRediT authorship contribution statement

Canyi Zhang: Writing – original draft, Visualization, Methodology, Formal analysis, Data curation. **Junhuai Yang:** Writing – review & editing, Supervision, Investigation, Funding acquisition, Formal analysis, Conceptualization. **Fuyuan Gao:** Investigation, Formal analysis, Data curation. **Haoyu Wang:** Investigation, Formal analysis, Data curation. **Linkai Wang:** Investigation, Formal analysis, Data curation. **Zhenqian Wang:** Resources, Methodology, Data curation. **Xin Liu:** Investigation, Formal analysis, Data curation. **Wenxi Qu:** Investigation, Formal analysis, Data curation. **Shuyuan Wang:** Investigation, Formal analysis, Data curation. **Zixuan Chen:** Investigation, Formal analysis, Data curation. **Youjun Wang:** Funding acquisition. **Fen Zhang:** Supervision. **Dunsheng Xia:** Supervision.

Declaration of competing interest

The authors declare that they have no known competing financial interests or personal relationships that could have appeared to influence the work reported in this paper.

Acknowledgements

This research was sponsored by the Postdoctoral Fellowship Program of CPSF (GZC20231004), the China Postdoctoral Science Foundation (2024T170369, 2024M751256), the Fundamental Research Funds for the Central Universities (lzujbky-2024-pd05), the Natural Science Foundation of Gansu Province (24JRRA471), the Open Foundation of MOE Key Laboratory of Western China's Environmental System, Lanzhou University and the Fundamental Research Funds for the Central

Universities (504000-561224013), the Science and Technology Major Project of Tibetan Autonomous Region of China (XZ202201ZD0005G01), and the Shandong Provincial Natural Science Foundation of China (ZR2021QD122). We thank the Editor-in-Chief Dr. Howard Falcon-Lang and three reviewers for their insightful comments and suggestions, which have improved the manuscript. We are grateful to Dr. Jan Bloemendal for improving the English.

Appendix A. Supplementary data

Supplementary data to this article can be found online at <https://doi.org/10.1016/j.palaeo.2025.113179>.

Data availability

All data used in this study can be found in the Mendeley data repository and are available at <https://data.mendeley.com/datasets/xb8ngwysm6/1>.

References

- Aitken, M.J., 1998. An Introduction to optical dating: the dating of Quaternary sediments by the use of photon-stimulated luminescence. Oxford University Press. <https://doi.org/10.1017/S0016756899551777>.
- Blaauw, M., Christen, J.A., 2011. Flexible paleoclimate age-depth models using an autoregressive gamma process. *Bayesian Anal.* 6 (3), 457–474. <https://doi.org/10.1214/ba/1339616472>.
- Blaauw, M., Christen, J.A., Bennett, K.D., Reimer, P.J., 2018. Double the dates and go for Bayes - Impacts of model choice, dating density and quality on chronologies. *Quat. Sci. Rev.* 188, 58–66. <https://doi.org/10.1016/j.quascirev.2018.03.032>.
- Blott, S.J., Pye, K., 2001. GRADISTAT: a grain size distribution and statistics package for the analysis of unconsolidated sediments. *Earth Surf. Process. Landf.* 26 (11), 1237–1248. <https://doi.org/10.1002/esp.261>.
- Chen, Y.W., Zong, Y.Q., Li, B., Li, S.H., Aitchison, J.C., 2013. Shrinking lakes in Tibet linked to the weakening Asian monsoon in the past 8.2 ka. *Quat. Res.* 80 (2), 189–198. <https://doi.org/10.1016/j.yqres.2013.06.008>.
- Chen, F.H., Chen, J.H., Huang, W., Chen, S.Q., Huang, X.Z., Jin, L.Y., Jia, J., Zhang, X.J., An, C.B., Zhang, J.W., Zhao, Y., Yu, Z.C., Zhang, R.H., Liu, J.B., Zhou, A.F., Feng, S., 2019. Westerlies Asia and monsoonal Asia: Spatiotemporal differences in climate change and possible mechanisms on decadal to sub-orbital timescales. *Earth Sci. Rev.* 192, 337–354. <https://doi.org/10.1016/j.earscirev.2019.03.005>.
- Chen, F.H., Zhang, J.F., Liu, J.B., Cao, X.Y., Hou, J.Z., Zhu, L.P., Xu, X.K., Liu, X.J., Wang, M.D., Wu, D., Huang, L.X., Zeng, T., Zhang, S., Huang, W., Zhang, X., Yang, K., 2020. Climate change, vegetation history, and landscape responses on the Tibetan Plateau during the Holocene: a comprehensive review. *Quat. Sci. Rev.* 243, 106444. <https://doi.org/10.1016/j.quascirev.2020.106444>.
- Chen, J.C., Xu, J.Z., Wu, Z.J., Meng, X.X.Y., Yu, Y., Ginoux, P., DeMott, P.J., Xu, R., Zhai, L.X., Yan, Y.F., Zhao, C.F., Li, S.M., Zhu, T., Hu, M., 2024. Decreased dust particles amplify the cloud cooling effect by regulating cloud ice formation over the Tibetan Plateau. *Sci. Adv.* 10 (37), ado0885. <https://doi.org/10.1126/sciadv.ado0885>.
- Cheng, L.Q., Song, Y.G., Chang, H., Li, Y., Orozbaev, R., Zeng, M.X., Liu, H.F., 2020. Heavy mineral assemblages and sedimentation rates of eastern Central Asian loess: Paleoenvironmental implications. *Paleogeogr. Paleoclimatol. Paleoecol.* 551, 109747. <https://doi.org/10.1016/j.palaeo.2020.109747>.
- Cheng, L.Q., Song, Y.G., Yang, L.H., Chang, H., Wu, Y.B., Long, H., Miao, X.D., Dong, Z.B., 2022. Variations of the intensity of the Siberian High during the last Glacial revealed by the sorting coefficient of loess-paleosol deposits in eastern Central Asia. *Paleoceanogr. Paleoclimatology* 37 (9), 11. <https://doi.org/10.1029/2022pa004468>.
- Cheng, L.Q., Yang, L.H., Long, H., Zhang, J.R., Miao, X.D., Wu, Y.B., Lan, M.W., Song, Y.G., Dong, Z.B., 2023. Late Holocene change in South Asian monsoons and their influences on human activities in the southern Tibetan Plateau. *Catena* 228, 107153. <https://doi.org/10.1016/j.catena.2023.107153>.
- Cheng, L.Q., Long, H., Yang, L.H., Zhang, J.R., Song, Y.G., Chen, Z., Wu, Y.B., Dong, Z.B., 2025. Mountain glaciers regulate the response of Tibetan Plateau dust activity to global climate change during the last glacial. *Quat. Sci. Rev.* 359, 109375. <https://doi.org/10.1016/j.quascirev.2025.109375>.
- Dong, G.C., Yi, C.L., Chen, L.J., 2010. An Introduction to the physical geography of the Qiangtang Plateau: a frontier for future geoscience research on the Tibetan Plateau. *Phys. Geogr.* 31 (6), 475–492. <https://doi.org/10.2747/0272-3646.31.6.475>.
- Dong, Z.B., Hu, G.Y., Qian, G.Q., Lu, J.F., Zhang, Z.C., Luo, W.Y., Lyu, P., 2017. High-altitude aeolian research on the Tibetan Plateau. *Rev. Geophys.* 55 (4), 864–901. <https://doi.org/10.1002/2017rg000585>.
- Duan, F.T., An, C.B., Wang, W., Herzschuh, U., Zhang, M., Zhang, H.X., Liu, Y., Zhao, Y.T., Li, G.Q., 2020. Dating of a late Quaternary loess section from the northern slope of the Tianshan Mountains (Xinjiang, China) and its paleoenvironmental significance. *Quat. Int.* 544, 104–112. <https://doi.org/10.1016/j.quaint.2020.02.034>.

- Duller, G.A.T., 2003. Distinguishing quartz and feldspar in single grain luminescence measurements. *Radiat. Meas.* 37 (2), 161–165. [https://doi.org/10.1016/s1350-4487\(02\)00170-1](https://doi.org/10.1016/s1350-4487(02)00170-1).
- Dyke, A.S., 2004. An outline of north American deglaciation with emphasis on central and northern Canada. *Develop. Quatern. Sci.* 2, 373–424. [https://doi.org/10.1016/S1571-0866\(04\)80209-4](https://doi.org/10.1016/S1571-0866(04)80209-4).
- Fang, X.M., Han, Y.X., Ma, J.H., Song, L.C., Yang, S.L., Zhang, X.Y., 2004. Dust storms and loess accumulation on the Tibetan Plateau: a case study of dust event on 4 March 2003 in Lhasa. *Chin. Sci. Bull.* 49 (9), 953–960. <https://doi.org/10.1360/03wd0180>.
- Folk, R.L., Ward, W.C., 1957. Brazos River bar: a study in the significance of grain size parameters. *J. Sediment. Res.* 27 (1), 3–26. <https://doi.org/10.1306/74D70646-2B21-11D7-8648000102C1865D>.
- Gao, F.Y., Zheng, X.M., Jia, J., Li, K.M., Xia, D.S., Yang, J.H., Lu, H., Shi, F.X., Chen, Z.X., Wang, S.Y., 2021. Evolution of near-surface wind strength in northeastern arid Central Asia during the Holocene. *Paleoceanogr. Paleoclimatology*. 36 (2), e2020PA003970. <https://doi.org/10.1029/2020PA003970>.
- Gao, F.Y., Yang, J.H., Wang, S.Y., Wang, Y.J., Li, K.M., Wang, F., Ling, Z.Y., Xia, D.S., 2022a. Variation of the winter mid-latitude Westerlies in the Northern Hemisphere during the Holocene revealed by aeolian deposits in the southern Tibetan Plateau. *Quat. Res.* 107, 104–112. <https://doi.org/10.1017/qua.2021.65>.
- Gao, F.Y., Yang, J.H., Xia, D.S., Lu, H., Wang, S.Y., Li, K.M., Wang, Z.Q., Wu, Z.P., Zhou, J.X., Shi, F.X., 2022b. Linking moisture and near-surface wind with winter temperature to reveal the Holocene climate evolution in arid Xinjiang region of China. *Geosci. Front.* 13 (6), 101433. <https://doi.org/10.1016/j.gsf.2022.101433>.
- Guijarro, J.A., 2018. Homogenization of climatic series with Climatol. In: State Meteorological Agency (AEMET), Balear Islands Office, Spain. <https://doi.org/10.13140/RG.2.2.27020.41604>.
- Guo, Z.T., Peng, S.Z., Hao, Q.Z., Biscaye, P.E., Liu, T.S., 2001. Origin of the Miocene-Pliocene red-earth formation at Xifeng in northern China and implications for paleoenvironments. *Paleogeogr. Paleoclimatol. Paleoecol.* 170 (1–2), 11–26. [https://doi.org/10.1016/s0031-0182\(01\)00235-8](https://doi.org/10.1016/s0031-0182(01)00235-8).
- Hudson, A.M., Quade, J., Huth, T.E., Lei, G.L., Cheng, H., Edwards, L.R., Olsen, J.W., Zhang, H.C., 2015. Lake level reconstruction for 12.8–2.3 ka of the Ngangla Ring Tso closed-basin lake system, southwest Tibetan Plateau. *Quat. Res.* 83 (1), 66–79. <https://doi.org/10.1016/j.yqres.2014.07.012>.
- Jia, J., Liu, H., Gao, F.Y., Xia, D.S., 2018. Variations in the westerlies in Central Asia since 16 ka recorded by a loess section from the Tien Shan Mountains. *Palaeogeogr. Palaeoclimatol. Palaeoecol.* 504, 156–161. <https://doi.org/10.1016/j.palaeo.2018.05.021>.
- Kang, S.C., Zhang, Y.L., Qian, Y., Wang, H.L., 2020. A review of black carbon in snow and ice and its impact on the cryosphere. *Earth Sci. Rev.* 210, 103346. <https://doi.org/10.1016/j.earscirev.2020.103346>.
- Kang, S.G., Wang, X.L., Du, J.H., Song, Y.G., 2022a. Paleoclimates inform on a weakening and amplitude-reduced East Asian winter monsoon in the warming future. *Geology* 50 (11), 1224–1228. <https://doi.org/10.1130/g50246.1>.
- Kang, S.G., Wang, X.L., Wang, N., Song, Y.G., Liu, W.G., Wang, D., Peng, J., 2022b. Siberian high modulated suborbital-scale dust accumulation changes over the past 30 ka in the eastern Yili Basin, Central Asia. *Paleoceanogr. Paleoclimatology*. 37 (5), e2021PA004360. <https://doi.org/10.1029/2021PA004360>.
- Lai, Z.P., 2006. Testing the use of an OSL Standardised Growth Curve (SGC) for D_e determination on quartz from the Chinese Loess Plateau. *Radiat. Meas.* 41 (1), 9–16. <https://doi.org/10.1016/j.radmeas.2005.06.031>.
- Lambert, F., Kug, J.S., Park, R.J., Mahowald, N., Winckler, G., Abe-Ouchi, A., O’Iishi, R., Takemura, T., Lee, J.H., 2013. The role of mineral-dust aerosols in polar temperature amplification. *Nat. Clim. Chang.* 3 (5), 487–491. <https://doi.org/10.1038/nclimate1785>.
- Lambert, F., Tagliabue, A., Shaffer, G., Lamy, F., Winckler, G., Farias, L., Gallardo, L., De Pol-Holz, R., 2015. Dust fluxes and iron fertilization in Holocene and last Glacial Maximum climates. *Geophys. Res. Lett.* 42 (14), 6014–6023. <https://doi.org/10.1002/2015gl064250>.
- Li, X.Z., Yi, C.L., Chen, F.H., Yao, T.D., Li, X., 2006. Formation of proglacial dunes in front of the Puruogangri Icefield in the Central Qinghai-Tibet Plateau: Implications for reconstructing paleoenvironmental changes since the Lateglacial. *Quat. Int.* 154, 122–127. <https://doi.org/10.1016/j.quaint.2006.02.006>.
- Ling, Z.Y., Yang, S.L., Wang, X., Wang, J.P., Xia, D.S., Chen, F.H., 2020. Spatial-temporal differentiation of aeolian sediments in the Yarlung Tsangpo catchment, Tibetan Plateau, and response to global climate change since the last Glaciation. *Geomorphology* 357, 107104. <https://doi.org/10.1016/j.geomorph.2020.107104>.
- Ling, Z.Y., Li, J.S., Jin, J.H., Wang, J.P., Kong, F.C., Chen, L., 2021. Geochemical characteristics and provenance of aeolian sediments in the Yarlung Tsangpo valley, Southern Tibetan Plateau. *Environ. Earth Sci.* 80 (18), 623. <https://doi.org/10.1007/s12665-021-09928-5>.
- Ling, Z.Y., Yang, S.L., Xia, D.S., Wang, X., Chen, F.H., 2022. Source of the aeolian sediments in the Yarlung Tsangpo valley and its potential dust contribution to adjacent oceans. *Earth Surf. Process. Landf.* 47 (7), 1860–1871. <https://doi.org/10.1002/esp.5351>.
- Ling, Z.Y., Yang, J.H., Wang, Z.Q., Jin, J.H., Xia, D.S., Yang, S.L., Wang, X., Chen, F.H., 2023. Spatiotemporal differences in Holocene climate change in the Yarlung Tsangpo catchment, southern Tibetan Plateau, reconstructed from two sandy loess sequences. *Paleogeogr. Paleoclimatol. Paleoecol.* 616, 111473. <https://doi.org/10.1016/j.palaeo.2023.111473>.
- Liu, L.N., 2023. Pollen-Based Reconstruction of Vegetation Cover for the Last 20,000 Years on the Central-Eastern Tibetan Plateau (in Chinese). Institute of Tibetan Plateau Research, Chinese Academy of Sciences, Beijing.
- Liu, Z., Otto-Biesner, B.L., He, F., Brady, E.C., Tomas, R., Clark, P.U., Carlson, A.E., Lynch-Stieglitz, J., Curry, W., Brook, E., Erickson, D., Jacob, R., Kutzbach, J., 2019. Optical dating of Holocene paleosol development and climate changes in the Yili Basin, arid Central Asia. *The Holocene* 29 (6), 1068–1077. <https://doi.org/10.1177/0959683619831432>.
- Cheng, J., 2009. Transient simulation of last Deglaciation with a new mechanism for Bolling-Allerod warming. *Science* 325 (5938), 310–314. <https://doi.org/10.1126/science.1171041>.
- Liu, S., Hu, K.H., Liu, W.M., Carling, P.A., 2022a. Hydro-climatic characteristics of Yarlung Zangbo River Basin since the last Glacial Maximum. *Adv. Atmos. Sci.* 39 (3), 415–426. <https://doi.org/10.1007/s00376-021-1150-7>.
- Liu, Y.Z., Huang, J.P., Wang, T.H., Li, J.M., Yan, H.R., He, Y.L., 2022b. Aerosol-cloud interactions over the Tibetan Plateau: An overview. *Earth Sci. Rev.* 234, 104216. <https://doi.org/10.1016/j.earscirev.2022.104216>.
- Liu, J.B., Chen, Z.T., Chen, S.Q., 2024a. Southward shift of the westerly jet intensified late Holocene dust storms on the Tibetan Plateau. *Glob. Planet. Chang.* 237, 104461. <https://doi.org/10.1016/j.gloplacha.2024.104461>.
- Liu, X., Yang, J.H., Zhao, L., Liu, Y., Gao, F.Y., Tang, J.M., Wang, H.Y., Chen, Z.X., Wang, S.Y., Li, G.H., Lu, H., Li, Z.J., Wang, F., Xia, D.S., 2024b. Aeolian activity in the Yarlung Zangbo River Basin, southern Tibetan Plateau, began at 584 ka: implications for the glaciation of the Tibetan Plateau. *Quat. Sci. Rev.* 337, 108799. <https://doi.org/10.1016/j.quascirev.2024.108799>.
- Long, H., Cheng, L.Q., Yang, F., Zhang, G.L., 2025. Temperature regulates dust activities over the Tibetan Plateau. *The Innovation* 6 (4), 100840. <https://doi.org/10.1016/j.xinn.2025.100840>.
- Lu, H.Y., An, Z.S., 1998. Paleoclimatic significance of grain size of loess-palaeosol deposit in Chinese Loess Plateau. *Sci. China Ser. D-Earth Sci.* 41 (6), 626–631. <https://doi.org/10.1007/bf02877845>.
- Mahowald, N., 2011. Aerosol indirect effect on biogeochemical cycles and climate. *Science* 334 (6057), 794–796. <https://doi.org/10.1126/science.1207374>.
- Murray, A.S., Wintle, A.G., 2000. Luminescence dating of quartz using an improved single-aliquot regenerative-dose protocol. *Radiat. Meas.* 32 (1), 57–73. [https://doi.org/10.1016/s1350-4487\(99\)00253-x](https://doi.org/10.1016/s1350-4487(99)00253-x).
- Pan, M.H., Wu, Y.Q., Zheng, Y.H., Tan, L.H., 2014. Holocene aeolian activity in the Dinggye area (Southern Tibet, China). *Aeolian Res.* 12, 19–27. <https://doi.org/10.1016/j.aeolia.2013.10.005>.
- Paterson, G.A., Heslop, D., 2015. New methods for unmixing sediment grain size data. *Geochem. Geophys. Geosyst.* 16 (12), 4494–4506. <https://doi.org/10.1002/2015GC006070>.
- Peng, F., Nie, J.S., Stevens, T., Pan, B.T., 2022. Decoupled Chinese Loess Plateau dust deposition and Asian aridification at millennial and tens of millennial timescales. *Geophys. Res. Lett.* 49 (20), e2022GL099338. <https://doi.org/10.1029/2022gl099338>.
- Prescott, J.R., Hutton, J.T., 1994. Cosmic ray contributions to dose rates for luminescence and ESR dating: large depths and long-term time variations. *Radiat. Meas.* 23 (2–3), 497–500. [https://doi.org/10.1016/1350-4487\(94\)90086-8](https://doi.org/10.1016/1350-4487(94)90086-8).
- Pye, K., 2015. Aeolian dust and dust deposits. Academic Press, London. <https://doi.org/10.1016/C2013-0-05007-4>.
- Qiu, J., 2008. The third pole. *Nature* 454 (7203), 393–396. <https://doi.org/10.1038/454393a>.
- Rades, E.F., Hetzel, R., Xu, Q., Ding, L., 2013. Constraining Holocene lake-level highstands on the Tibetan Plateau by ^{10}Be exposure dating: a case study at Tangra Yumco, southern Tibet. *Quat. Sci. Rev.* 82, 68–77. <https://doi.org/10.1016/j.quascirev.2013.09.016>.
- Rades, E.F., Tsukamoto, S., Frechen, M., Xu, Q., Ding, L., 2015. A lake-level chronology based on feldspar luminescence dating of beach ridges at Tangra Yum Co (southern Tibet). *Quat. Res.* 83 (3), 469–478. <https://doi.org/10.1016/j.yqres.2015.03.002>.
- Reimer, P.J., Austin, W.E.N., Bard, E., Bayliss, A., Blackwell, P.G., Ramsey, C.B., Butzin, M., Cheng, H., Edwards, R.L., Friedrich, M., Grootes, P.M., Guilderson, T.P., Hajdas, I., Heaton, T.J., Hogg, A.G., Hughen, K.A., Kromer, B., Manning, S.W., Muscheler, R., Palmer, J.G., Pearson, C., van der Plicht, J., Reimer, R.W., Richards, D.A., Scott, E.M., Southon, J.R., Turney, C.S.M., Wacker, L., Adolphi, F., Büntgen, U., Capron, M., Fahrni, S.M., Fogtmann-Schulz, A., Friedrich, R., Köhler, P., Kudsk, S., Miyake, F., Olsen, J., Reinig, F., Sakamoto, M., Sookdeo, A., Talamo, S., 2020. The IntCal20 Northern Hemisphere radiocarbon age calibration curve (0–55 cal kBP). *Radiocarbon* 62 (4), 725–757. <https://doi.org/10.1017/rdc.2020.41>.
- Shaffer, G., Lambert, F., 2018. In and out of glacial extremes by way of dust-climate feedbacks. *Proc. Natl. Acad. Sci. USA* 115 (9), 2026–2031. <https://doi.org/10.1073/pnas.1708174115>.
- Song, Y.G., Wei, H.R., Xie, M.P., Kang, S.G., Zong, X.L., Shukurov, N., Shukurov, S., Li, Y., Li, Y., Zhang, M.Y., 2024. New insights into Holocene dust activity in eastern Uzbekistan. *Glob. Planet. Chang.* 243, 104633. <https://doi.org/10.1016/j.gloplacha.2024.104633>.
- Stauch, G., 2015. Geomorphological and palaeoclimate dynamics recorded by the formation of aeolian archives on the Tibetan Plateau. *Earth Sci. Rev.* 150, 393–408. <https://doi.org/10.1016/j.earscirev.2015.08.009>.
- Sun, J.M., Li, S.H., Muhs, D.R., Li, B., 2007. Loess sedimentation in Tibet: provenance, processes, and link with Quaternary glaciations. *Quat. Sci. Rev.* 26 (17–18), 2265–2280. <https://doi.org/10.1016/j.quascirev.2007.05.003>.
- Tsoar, H., Pye, K., 1987. Dust transport and the question of desert loess formation. *Sedimentology* 34 (1), 139–153. <https://doi.org/10.1111/j.1365-3091.1987.tb00566.x>.
- Vandenberge, J., 2013. Grain size of fine-grained windblown sediment: a powerful proxy for process identification. *Earth Sci. Rev.* 121, 18–30. <https://doi.org/10.1016/j.earscirev.2013.03.001>.
- Wang, L.B., Jia, J., Zhao, H., Liu, H., Duan, Y.W., Xie, H.C., Zhang, D.D., Chen, F.H., 2019. Optical dating of Holocene paleosol development and climate changes in the Yili Basin, arid Central Asia. *The Holocene* 29 (6), 1068–1077. <https://doi.org/10.1177/0959683619831432>.

- Wang, B.N., Gong, J.F., Zuza, A.V., Liu, R., Bian, S., Tian, Y.H., Yang, X.P., Zhang, D.G., Chen, H.L., 2021a. Aeolian sand dunes alongside the Yarlung River in southern Tibet: a provenance perspective. *Geol. J.* 56 (5), 2625–2636. <https://doi.org/10.1002/gj.4058>.
- Wang, T.H., Tang, J.Y., Sun, M.X., Liu, X.W., Huang, Y.X., Huang, J.P., Han, Y., Cheng, Y.F., Huang, Z.W., Li, J.M., 2021b. Identifying a transport mechanism of dust aerosols over South Asia to the Tibetan Plateau: a case study. *Sci. Total Environ.* 758, 143714. <https://doi.org/10.1016/j.scitotenv.2020.143714>.
- Wang, H.Y., Yang, J.H., Gao, F.Y., Wang, S.Y., Wang, Z.Q., Qu, W.X., Li, J.Y., Liu, X., Zhang, C.Y., Wang, L.K., Fan, Y.J., Yang, S.L., Xia, D.S., 2024. Middle to late Holocene climate change in the monsoon-dominated southeastern Tibetan Plateau and its relationship with human activity. *Paleogeogr. Paleoclimatol. Paleoecol.* 645, 112209. <https://doi.org/10.1016/j.palaeo.2024.112209>.
- Weltje, G.J., 1997. End-member modeling of compositional data: Numerical-statistical algorithms for solving the explicit mixing problem. *Math. Geol.* 29 (4), 503–549. <https://doi.org/10.1007/bf02775085>.
- Wu, D., Ma, X.Y., Yuan, Z.J., Hillman, A.L., Zhang, J.W., Chen, J.H., Zhou, A.F., 2022. Holocene hydroclimatic variations on the Tibetan Plateau: An isotopic perspective. *Earth Sci. Rev.* 233, 104169. <https://doi.org/10.1016/j.earscirev.2022.104169>.
- Xu, C., Ma, Y.M., Yang, K., You, C., 2018. Tibetan Plateau impacts on global dust transport in the upper troposphere. *J. Clim.* 31 (12), 4745–4756. <https://doi.org/10.1175/jcli-d-17-0313.1>.
- Yan, Q., Owen, L.A., Zhang, Z., Jiang, N., Zhang, R., 2020. Deciphering the evolution and forcing mechanisms of glaciation over the Himalayan-Tibetan orogen during the past 20,000 years. *Earth Planet. Sci. Lett.* 541, 116295. <https://doi.org/10.1016/j.epsl.2020.116295>.
- Yang, J.H., Xia, D.S., Wang, S.Y., Wang, W.D., Ma, X.Y., Chen, Z.X., Gao, F.Y., Ling, Z.Y., Dong, Z.B., 2020. Near-surface wind environment in the Yarlung Zangbo River basin, southern Tibetan Plateau. *J. Arid. Land* 12 (6), 917–936. <https://doi.org/10.1007/s40333-020-0104-8>.
- Yang, J.H., Xia, D.S., Gao, F.Y., Wang, S.Y., Li, D.X., Fan, Y.J., Chen, Z.X., Tian, W.D., Liu, X.Y., Sun, X.Y., Wang, Z.Q., Wang, F., 2021. Holocene moisture evolution and its response to atmospheric circulation recorded by aeolian deposits in the southern Tibetan Plateau. *Quat. Sci. Rev.* 270, 107169. <https://doi.org/10.1016/j.quascirev.2021.107169>.
- Yang, J.H., Xia, D.S., Chen, Z.X., Wang, S.Y., Gao, F.Y., Liu, X., Zhao, S., Zhao, L., Liu, Y., 2023. Differentiating detrital and pedogenic contributions to the magnetic properties of aeolian deposits in the southern Tibetan Plateau: Implications for paleoclimatic reconstruction. *Catena* 220, 106736. <https://doi.org/10.1016/j.catena.2022.106736>.
- Yang, J.H., Wang, H.Y., Gao, F.Y., Wang, Z.Q., Wang, S.Y., Fan, Y.J., Li, T.Y., Liu, X., Qu, W.X., Li, J.Y., Zhang, Y.X., Chen, Z.X., Liu, L., Ayyamperumal, R., Yang, S.L., Xia, D.S., 2024. Holocene forcing of aeolian dust activity over the Tibetan Plateau and its surroundings. *Glob. Planet. Chang.* 235, 104400. <https://doi.org/10.1016/j.gloplacha.2024.104400>.
- Yang, J.H., Chen, S.Q., Ling, Z.Y., Zhang, C.Y., Wang, L.K., Wang, H.Y., Wang, S.Y., Gao, F.Y., Lizaga, I., Wang, F., Yang, S.L., Chen, F.H., 2025. Spatiotemporal evolution of aeolian sedimentary landscapes on the southern Tibetan Plateau during the late Quaternary: a review and recent advances. *Earth Sci. Rev.* 261, 105035. <https://doi.org/10.1016/j.earscirev.2024.105035>.
- Yao, T.D., Li, Z.G., Yang, W., Guo, X.J., Zhu, L.P., Kang, S.C., Wu, Y.H., Yu, W.S., 2010. Glacial distribution and mass balance in the Yarlung Zangbo River and its influence on lakes. *Chin. Sci. Bull.* 55 (20), 2072–2078. <https://doi.org/10.1007/s11434-010-3213-5>.
- Zan, J.B., Maher, B.A., Yamazaki, T., Fang, X.M., Han, W.X., Kang, J., Hu, Z., 2023. Mid-Pleistocene links between Asian dust, Tibetan glaciers, and Pacific iron fertilization. *Proc. Natl. Acad. Sci. USA* 120 (24), e2304773120. <https://doi.org/10.1073/pnas.2304773120>.
- Zhang, G.F., Azorin-Molina, C., Chen, D.L., McVicar, T.R., Guijarro, J.A., Deng, K.Q., Minola, L., Lee, J., Son, S.W., Ma, H., Shi, P.J., 2024a. Variability and trends of near-surface wind speed over the Tibetan Plateau: the role played by the westerly and Asian monsoon. *Adv. Clim. Chang. Res.* 15 (3), 525–536. <https://doi.org/10.1016/j.accre.2024.04.007>.
- Zhang, Z.D., Liang, J.N., Ji, H.Y., Li, M.Q., Ding, J., Tang, C.G., Zhang, M., Yu, Z.R., Cao, X.J., Tian, P.F., Ren, Y., Zhang, L., 2024b. Quantifying mineral dust emissions on the Tibetan Plateau with a modified dust source map. *Geophys. Res. Lett.* 51 (1), e2023GL107042. <https://doi.org/10.1029/2023gl107042>.
- Zhao, S., Xia, D.S., Jin, H.L., Jia, J., Li, G.H., Gao, F.Y., Wang, Y.J., 2016. Long-term weakening of the East Asian summer and winter monsoons during the mid- to late Holocene recorded by aeolian deposits at the eastern edge of the Mu Us Desert. *Paleogeogr. Paleoclimatol. Paleoecol.* 457, 258–268. <https://doi.org/10.1016/j.palaeo.2016.06.011>.
- Zhao, S., Xia, D.S., Lu, K.X., 2022. Holocene aeolian dust accumulation rates across the Chinese Loess Plateau. *Glob. Planet. Chang.* 208, 103720. <https://doi.org/10.1016/j.gloplacha.2021.103720>.